

Spin Chern insulator in a phononic fractal lattice

Pengtao Lai,¹ Hui Liu,^{1,*} Boyang Xie,¹ Weiyin Deng,² Haonan Wang,¹ Hua Cheng,^{1,†}
Zhengyou Liu,^{2,‡} and Shuqi Chen^{1,3,4,§}

¹*The Key Laboratory of Weak Light Nonlinear Photonics, Ministry of Education, School of Physics and TEDA Institute of Applied Physics, Nankai University, Tianjin 300071, China*

²*Key Laboratory of Artificial Micro- and Nanostructures of Ministry of Education and School of Physics and Technology, Wuhan University, Wuhan 430072, China*

³*School of Materials Science and Engineering, Smart Sensing Interdisciplinary Science Center, Nankai University, Tianjin 300350, China*

⁴*The Collaborative Innovation Center of Extreme Optics, Shanxi University, Taiyuan, Shanxi 030006, China*



(Received 7 January 2024; revised 18 March 2024; accepted 29 March 2024; published 24 April 2024)

The spin Chern topological phases are more natural in solid-state systems and are thought to exist in two or three dimensions. To date, there is no evidence for the existence of spin Chern topological phase in non-integer dimension. Fractal offers a platform for exploring novel topological phases and phenomena in noninteger dimension. Here, based on a phononic fractal lattice, we experimentally demonstrate the presence of the spin Chern phase in noninteger dimension. We find that the spin Chern phase is compressed in the fractal lattice compared to the crystal lattice. We also highlight the robustness and unidirectionality of spin-polarized topologically protected edge states even the momentum space is ill defined. Interestingly, sound travels faster at the boundaries of the fractal lattice than in crystal lattice. Abundant spin-polarized edge states and increased velocities not only may inspire further study in other noninteger dimensional systems, but also provide an opportunity for the design of multichannel on-chip communication devices.

DOI: [10.1103/PhysRevB.109.L140104](https://doi.org/10.1103/PhysRevB.109.L140104)

Introduction. A fractal, a shape that exhibits self-similarity and fractional dimension, is made of parts that are similar to the whole in some way [1]. Fractals are not only prevalent in nature such as the spatial distribution of the alexite in a salt flat [2], organ arrangement in cauliflower [3], or the growth of electrodeposits [4], but also inspired various promising applications such as fractal antennas [5,6] and fractal capacitors [7]. In physics, fractal plays a key role in investigating the novel physical properties and phenomena in noninteger dimensions, which greatly enriches the physical connotation. Classical transport in the fractional dimension has been extensively studied, and then the researches extend to quantum transport [8,9]. While the mean square displacement of quantum transport in regular lattices scales linearly, the experimental observation in the fractional dimension reveals an anomalous transport where the mean square displacement is exponentially related to the fractal dimension [10]. Recently, the quantum transport of topological edge states in fractals has attracted a lot of interest. Fractal systems do not contain any conventional bulk and thus fail to follow the bulk-edge correspondence that is the heart of topological theory. However, recent research has demonstrated that a photonic Floquet topological insulator can support a Chern

topological phase and chiral topological states in fractal lattice without well-defined bulk bands [11]. Even more interesting was found in the experimental observation, that is the increased velocity of the chiral edge state in the photonic fractal system [12]. Compared with the integer dimensions, the regions of the topological phase are compressed in the fractal lattice [13–17]. To date, research on the novel quantum transport phenomena in fractal systems has been limited to Chern, higher-order, and anomalous Floquet topological phases [18–22]. Further research and observations are needed to reveal the mechanism and the influence of fractal on various topological phases and states.

The quantum spin Hall effect is a well-known topological phase characterized by Z_2 topological invariant or spin Chern number [23–25]. It features pairs of spin-dependent edge states in the band gap [26–29]. Even when the spin conservation and time-reversal symmetry are broken by spin-mixing term, the quantum transport in periodic systems remains robust [30,31] and spin Chern numbers are still well defined [32,33]. This gives rise to the concept of spin Chern insulators [30,34–36]. However, most studies on spin Chern insulators have focused on integer dimensions. A recent observation of Sierpinski bismuth films suggests that fractal structure will close the quantum spin Hall effect due to the lack of a well-defined bulk [17]. Up to now, there is no evidence supporting the existence of a spin Chern phase in the fractal lattice.

In this letter, we report the observation of a spin Chern insulator in a phononic fractal lattice of the Sierpinski carpet. By capturing the topology with the real-space topological

*hliu@nankai.edu.cn

†hcheng@nankai.edu.cn

‡zylu@whu.edu.cn

§schen@nankai.edu.cn

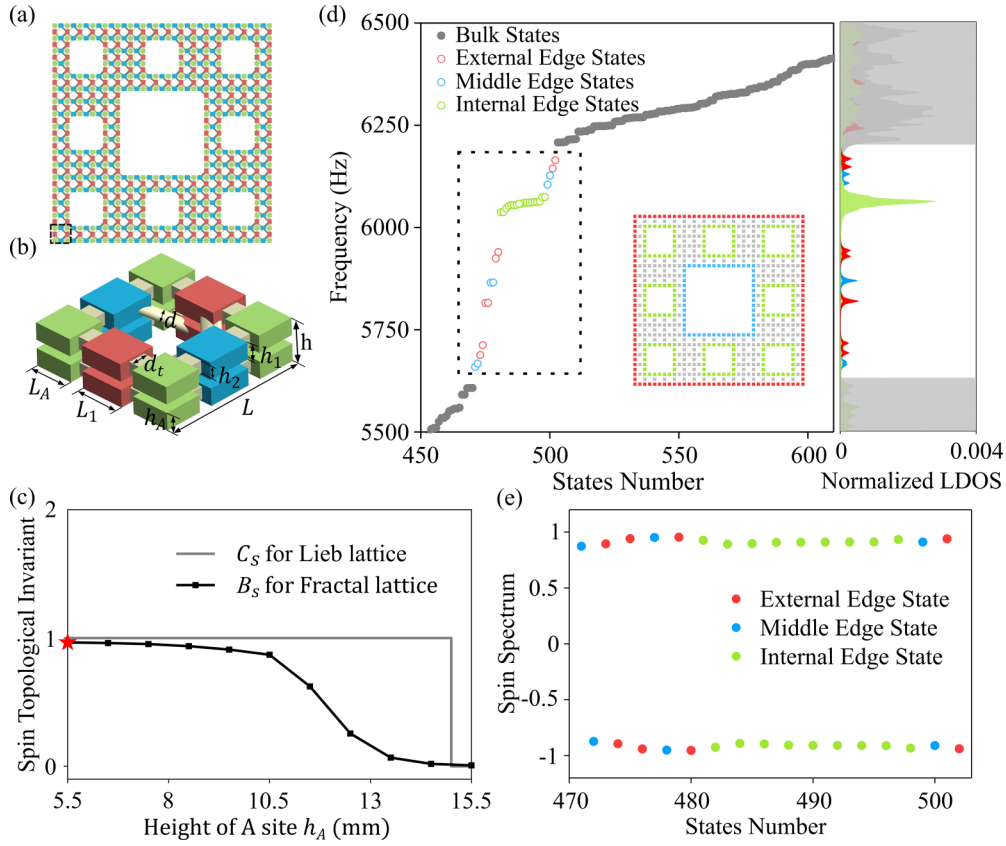


FIG. 1. Fractal spin Chern insulator and spin-polarized edge states. (a) Top view of G(2) fractal lattice. The green, blue, and red cavities denote A, B, and C sites. (b) The structure details of the fractal lattice. (c) Compared with the spin Chern number C_S in Lieb lattice, the topological phase in the fractal lattice, which is characterized by the spin Bott index B_S is compressed. (d) (Left) Numerically calculated energy spectrum of the fractal lattice. The mid-gap presents a hierarchy of edge states including external, middle, and internal edge states. (Inset) Spatial distribution of the bulk (grey), external edge (red), middle edge (blue), and internal edge (green). (Right) Calculated localized density of states. (e) Calculated spin spectrum of the edge states in the gap.

invariant, the spin Bott index, we observe the topological nontrivial phase in the compressed topological phase range. Furthermore, we observed the propagation of pseudospin-polarized edge states in the fractal lattice, which is not only more abundant but also has a similar behavior to the “spin-momentum locking” in crystalline structures. Although the boundary is easy to be truncated by defects in the fractal lattice, which seems to undermine the robustness of topological edge states, our experimental observation shows that the sound would go smoothly around the defect through the internal edge. By extracting the transmission velocity of sound waves at the boundaries, we further confirm that sound travels faster at the boundaries of the fractal lattice compared to the crystal lattice.

Model and methods. The Sierpinski carpet is one of the most famous deterministic fractals with the Hausdorff dimension $d = \frac{\log 8}{\log 3} \cong 1.89$. Taking the bilayer Lieb lattice into account, the Sierpinski carpet can be generated through an iterative process that starts by dividing a square Lieb lattice into nine equal parts, removing the central part, and using the remaining eight smaller parts for further iteration. The second generation [G(2)] of the Sierpinski carpet is depicted in Fig. 1(a), where the phononic crystal has three different sites, labeled A (green), B (blue), and C (red), in each layer.

The structural details of the Sierpinski carpet are shown in Fig. 1(b), which has in-plane length $L = 29.7$ mm and height $h = 13.75$ mm. The heights of A, B, and C cavities are $h_A = 5.5$ mm and $h_B = h_C = h_1 = 5.5$ mm. The lengths of three cavities are $L_A = 7.7$ mm and $L_B = L_C = L_1 = 8.8$ mm, respectively. The height and width of the tubes for the intralayer couplings are $h_2 = 3.96$ mm and $d_t = 3.52$ mm. The diameter of the tubes for the interlayer couplings is $d = 3.52$ mm.

In the phononic crystal, the eigenoscillation mimics the wave function, and cavities play the role of the lattice sites. The tubes connecting different cavities introduce the hopping parameters. As bilayer Lieb lattices provide a layer degree of freedom, in the basis of $(A_{1\uparrow}, B_{1\uparrow}, C_{1\uparrow}, \dots, A_{N\uparrow}, B_{N\uparrow}, C_{N\uparrow}, A_{1\downarrow}, B_{1\downarrow}, C_{1\downarrow}, \dots, A_{N\downarrow}, B_{N\downarrow}, C_{N\downarrow})$, where N represents the N th site and \uparrow / \downarrow stands for the upper/lower layer, the real-space Hamiltonian can be expressed in the form

$$H = \begin{pmatrix} H_{\text{intra}} & H_{\text{inter}} \\ H_{\text{inter}}^\dagger & H_{\text{intra}} \end{pmatrix}. \quad (1)$$

Here H_{intra} is a $N \times N$ matrix, containing on-site energy of N sites and intralayer couplings in each layer. H_{inter} is also a $N \times N$ matrix, which describes the interlayer couplings. By

performing a unitary transformation $U = \frac{1}{\sqrt{2}} \begin{pmatrix} 1 & -i \\ 1 & i \end{pmatrix} \otimes I_N$, where I_N is the $N \times N$ identity matrix, the basis can be transformed to $(A_{1\uparrow} - iA_{1\downarrow}, B_{1\uparrow} - iB_{1\downarrow}, C_{1\uparrow} - iC_{1\downarrow}, \dots, A_{N\uparrow} - iA_{N\downarrow}, B_{N\uparrow} - iB_{N\downarrow}, C_{N\uparrow} - iC_{N\downarrow}, A_{1\uparrow} + iA_{1\downarrow}, B_{1\uparrow} + iB_{1\downarrow}, C_{1\uparrow} + iC_{1\downarrow}, \dots, A_{N\uparrow} + iA_{N\downarrow}, B_{N\uparrow} + iB_{N\downarrow}, C_{N\uparrow} + iC_{N\downarrow})$. $(A_{n\uparrow} - iA_{n\downarrow}, B_{n\uparrow} - iB_{n\downarrow}, C_{n\uparrow} - iC_{n\downarrow})$ and $(A_{n\uparrow} + iA_{n\downarrow}, B_{n\uparrow} + iB_{n\downarrow}, C_{n\uparrow} + iC_{n\downarrow})$, where $n = 1, \dots, N$ represent the basis of pseudospin-up and pseudospin-down subspace, respectively. Under the unitary transformation, Hamiltonian H can be transformed into $H_u = UHU^\dagger$. The resulting Hamiltonian is

$$H_u = \frac{1}{2} \begin{pmatrix} 2H_{\text{intra}} + H_{\text{soc}} & H_{\text{mix}} \\ H_{\text{mix}}^\dagger & 2H_{\text{intra}} - H_{\text{soc}} \end{pmatrix}. \quad (2)$$

$H_{\text{soc}} = i(H_{\text{inter}} - H_{\text{inter}}^\dagger)$ has the form of spin-orbital coupling that open topological gaps, and the off-diagonal term $H_{\text{mix}} = -i(H_{\text{inter}} + H_{\text{inter}}^\dagger)$ represents the spin-mixing term that breaks spin conservation. The spin operator of the original Hamiltonian H can be expressed as $S_y = U^\dagger(\sigma_z \otimes I_N)U = \sigma_y \otimes I_N$, where $S_z = \sigma_z \otimes I_N$ is the spin operator of H_u .

Although the spin operator S_y does not commute with the Hamiltonian H due to the broken of spin conservation, it is still possible to decompose the projection operator of the occupied states P into two parts P_+ and P_- , which satisfy $P = P_+ \oplus P_-$. The projection operator P can be defined as

$$P = \sum_i^\alpha |\Psi_i\rangle \langle \Psi_i|. \quad (3)$$

When the spin-mixing term is not strong, the spin spectrum calculated by the eigenvalues of PS_yP contains two isolated parts, which are close to $+1$ and -1 and represent spin-up and spin-down sectors, respectively. As long as the spin mixing is not strong enough to close the spin spectrum gap, P_+ and P_- corresponding to the positive and negative sections can still be constructed as

$$P_\pm = \sum_i^{\alpha/2} |\pm\Psi_i\rangle \langle \pm\Psi_i|, \quad (4)$$

where $|\pm\Psi_i\rangle$ are the eigenstates of PS_yP with positive and negative eigenvalues.

As the translational symmetry is broken in the fractal lattice, the momentum-space spin Chern number C_s cannot be applied to characterize the topological phase in the fractal lattice. Here we employ the real-space spin Bott index B_s to characterize the topological phase of fractal lattice [37–39]. Based on the spin-dependent projection P_\pm , we can calculate the Bott index B_\pm for each spin sector. The spin Bott index can be calculated as $B_s = \frac{1}{2}(B_+ - B_-)$, which is robust until one of the two gaps closes: the energy gap of the Hamiltonian or the spin spectrum gap. More details about the calculation of spin Bott index are discussed in the Note I within the Supplemental Material (SM) [40]. The calculated spin Chern number and spin Bott index for the Lieb lattice [34] and G(2) Sierpinski carpet, respectively, are plotted as a function of the height of A sites h_A in Fig. 1(c). Besides the on-site term, the variation of height of A sites h_A also inevitably leads to slight changes in intralayer and interlayer couplings, but this does not prevent us from analyzing the topological phase transition. The spin Bott index is equivalent to the spin

Chern number in an infinite system. However, the difference between the spin Chern number and spin Bott index is within a correction of the order $O(1/L)$ in a finite system, where L is the system size [38,39]. As the gap decreases to zero near the phase transition point and the correlation length increases sharply, a larger sample size is required to achieve a higher Bott index calculation accuracy. Although the finite size of G(2) Sierpinski carpet induces a small deviation of spin Bott index at the phase transition point, this does not prevent us from distinguishing topological trivial and nontrivial phases. In the Lieb lattice, the lowest band gap closes at $h_A = 15$ mm, which is accompanied by the topological phase transition of the lowest two bands (see Note II within the SM [40] for the topological phase of Lieb lattice). For the fractal lattice, the topological phase transition is characterized by the spin Bott index. Removing the bulk sites will destroy the topology at the boundary of topological region, resulting in the compression of topological region. Similar phenomenon has been reported in Chern [16] and high-order [21] topological fractal systems.

Experiment realization in a phononic crystal. Here, we take $h_A = 5.5$ mm, with nontrivial spin Bott index denoted by the red star in Fig. 1(c). The energy spectrum of the G(2) Sierpinski carpet is shown in the left panel of Fig. 1(d). The bulk states (represented by grey dots) exhibit a large central gap with external, middle, and internal edge states within it, while only external edge states are present in the crystal lattice. The spatial distribution of the bulk (grey), external edge (red), middle edge (blue), and internal edge (green) is shown in the inset. The calculated local density of states (LDOS) is shown in the right panel of Fig. 1(d). The salient green peak at around 6060 Hz is caused by a group of internal edge states. The spin spectrum of edge states is depicted in Fig. 1(e), which slightly deviates from ± 1 due to the broken spin conservation. The spin spectrum of edge states consists of two isolated groups with opposite signs, allowing the edge states to be equally divided into two spin sectors. Higher-order generation of Sierpinski carpet shows a similar result that the edge states are self-similarly distributed. As the emergence of more edges in the iterative process, more edge states appear in the gap (see Note III within the SM [40] for details).

We now observe the abundant edge states in the fractal lattice and experimentally demonstrate their robustness. Figure 2(a) shows the phononic crystal sample fabricated by 3D printing technology with a defect that truncates the outer perimeter. Figures 2(c)–2(e) show the measured field profiles of middle, external, and internal edge states of G(2) Sierpinski carpet at 5868 Hz, 6150 Hz, and 6050 Hz, respectively. The sound source is placed at the pink star in the upper layer, and a sound probe (B&K Type 4961) is used to detect the sound pressure in the upper layer. It can be seen that the sound pressure is well confined at the edges of Sierpinski carpet, which corresponds well with the simulation result in Note III within the SM [40]. The sound intensity attenuates during its propagation due to the inevitable loss in the air. As there is no well-defined bulk in the fractal lattice, its edge is easy to be truncated when defects are considered. In Fig. 2(f), we introduce a defect that truncates the outer perimeter and then excites the external edge state to verify the robustness of edge state. The experimental result shows that the sound propagates smoothly through the internal edge to make a detour around

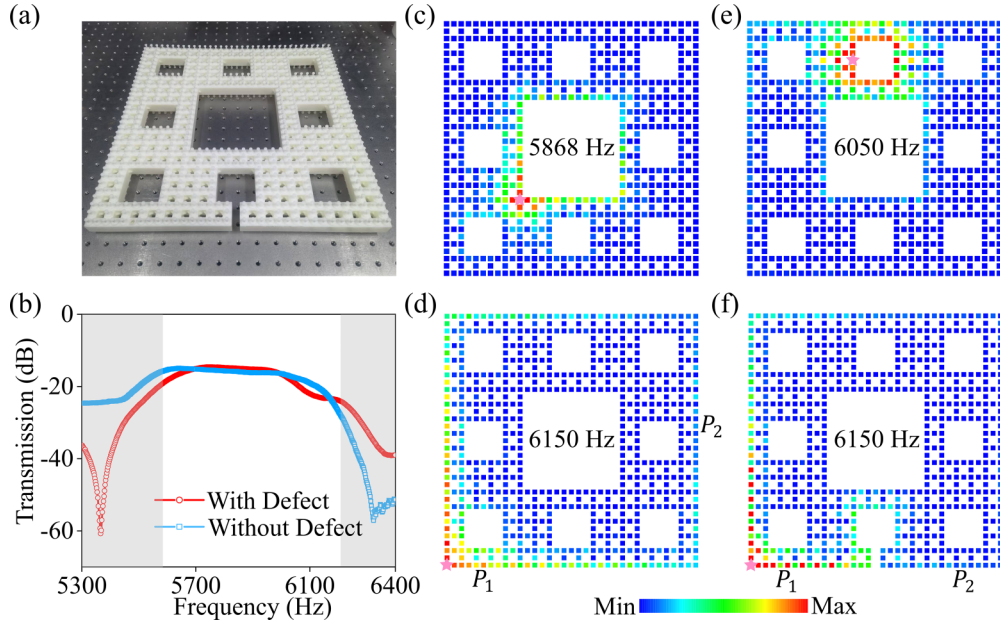


FIG. 2. Robustness of topological edge states against defect. (a) Photograph of Sierpinski carpet sample with defect at the outer perimeter. (b) Measured transmission spectra for the sample with and without a defect. (c)–(e) Measured field intensity profiles for the (c) middle, (d) external, and (e) internal edge state at 5868 Hz, 6150 Hz, and 6050 Hz, respectively. (f) Measured field intensity profiles for the external edge state with a defect at 6150 Hz.

the defect. Moreover, we measure the transmission spectra from P_1 point to P_2 point, as plotted in Fig. 2(b). For comparison, the distance between the P_1 point and P_2 point in Fig. 2(f) is kept the same as that in Fig. 2(d). The transmission spectra of two samples agree well with each other in the gap, which indicates the robustness of edge states.

To further verify the transmission characteristics of the pseudospin-polarized edge states, we selectively excite edge states with different pseudospins and investigate their temporal dynamics. The spin-polarized edge states can be characterized by the spin operator S_y . The two eigenvectors of σ_y with eigenvalue ∓ 1 are $1/\sqrt{2}[\pm i, 1]^T$. According to these eigenvectors, we launch a Gaussian wave packet at the cyan star in Fig. 3(a), which can be expressed as $[A_\uparrow, A_\downarrow]^T = A(t)[\pm i, 1]^T$ with $A(t) = e^{-(\frac{t-t_0}{\sigma})^2} \sin(2\pi f_c t)$. Here, A_\uparrow (A_\downarrow) represents the amplitude of the source in the upper (lower) layer. The time delay is set to $t_0 = 10$ ms, and the packet width is $\sigma = 0.5$ ms. To extract sound velocities with different pseudospins from the same boundary, we place the sound source at two end points of external Edge 1 and measure the movement of the wave packet with different pseudospins on it, respectively. To avoid exciting their neighboring edge states, we place the sound source at the corner and the middle of the boundary for the middle and internal edge states, respectively. The central frequencies f_c are 6150 Hz, 5868 Hz, and 6050 Hz for the external [Figs. 3(d) and 3(g)], middle [Figs. 3(e) and 3(h)], and internal [Figs. 3(f) and 3(i)] edge states, respectively.

The evolution of spin-down-polarized wave packets, which are measured along the counterclockwise direction, are shown in Figs. 3(d)–3(f), respectively. In the external edge [Fig. 3(d)] the spin-down wave packet propagates clockwise, while in the

inner edge [including middle edge Fig. 3(e) and internal edge Fig. 3(f)] wave packet propagates counterclockwise (see Note V within the SM [40]). The spin-up-polarized wave packets in Figs. 3(g)–3(i) flow in the opposite direction from their spin-down counterparts. In the Sierpinski carpet, the propagating direction of edge states is locking with the spin, which is similar to “spin-momentum locking” in the spin Chern insulator. Since the sound signals are measured along the entire middle and internal edges, the noise modes, such as the sound source mode, are captured near the source, resulting in small bifurcations propagating in the opposite directions. The noisy modes, which are not protected by the topology, attenuate quickly around the 90° corner, leading to a better unidirectional behavior in Figs. 3(f) and 3(i) than Figs. 3(e) and 3(h). To study the robustness of topological edge modes against a 90° sharp corner, we extract the signal wave packet at points A, B, C, and D at the middle edge. As depicted in Fig. 3(b), it is confirmed that there is one-way transport of the signal with little backscattering from the sharp corner, and the attenuation of the amplitude is mainly attributed to the loss in air.

The transmission velocity of sound waves at the boundaries is calculated as the linear regression slope of the position and the arrival time (see Note IV within the SM [40] for more details). To extract the center of Gaussian type envelope, we applied a Gaussian fit to the envelope of the wave packet. The central frequency of source is set at the center of the gap, i.e., $f_c = 6000$ Hz, to minimize the excitation of bulk states. A Lieb lattice sample with the same size as the G(2) Sierpinski carpet sample was fabricated and measured for comparison (see SM [40]). As shown in Fig. 3(c), both the spin-up and -down Gaussian wave packet in fractal lattice exhibit higher transmission velocities, approximately 12%, than that in the Lieb lattice, which are

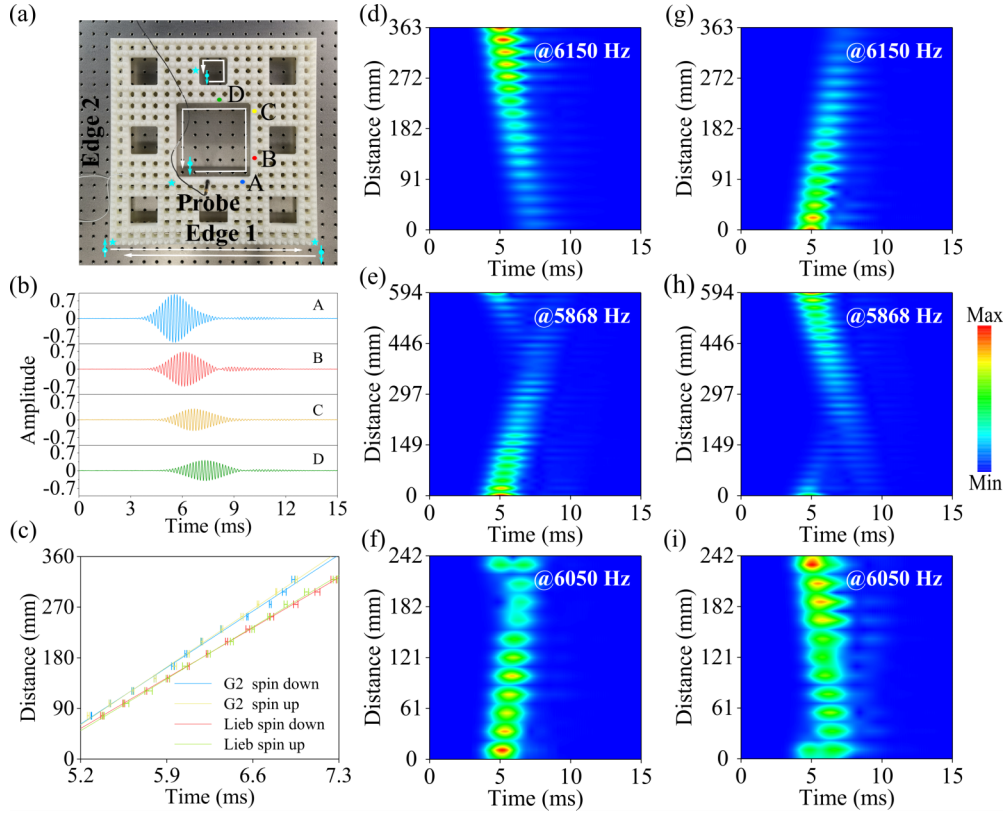


FIG. 3. Experimental observation of spin-dependent edge transport with Gaussian pulse excitation. (a) The sample photo of phononic fractal lattice. Cyan stars and white arrows represent the acoustic sources and the propagating directions for different pseudospin states, respectively. (b) Measured wave packets at points A, B, C, and D in (a). (c) Comparison of edge state velocities in the fractal lattice with that in crystalline counterpart. The fitted velocities of spin-down/up-polarized edge states in the fractal and crystal lattice are 143.2 m/s, 146.9 m/s, 127.7 m/s, and 131.6 m/s, respectively. (d)–(i) Envelopes of propagating pulses in the space-time domain which is measured along the counterclockwise direction, where (d)–(f) and (g)–(i) show the edge states excited by spin down and up source, respectively. The external, middle, and internal edge states are excited by the Gaussian pulses at center frequencies of 6150 Hz, 5868 Hz, and 6050 Hz, respectively.

similar to previous results in photonic Floquet systems [12]. The external edges are close to the middle and internal edges in the fractal lattice, introducing the finite size effect of the edge state, which leads to the increase of velocity in boundary [29] (details can be found in Note VI within the SM [40]). The difference in velocities between two spin-polarized wave packets in the fractal lattice is relatively small (less than 3%) and within the margin of experimental error.

Conclusions. In summary, we reported on the observation of the spin Chern insulator in a fractal lattice. Compared to the crystal lattice, the topological phase of fractal lattice, characterized by the real-space spin Bott index, is compressed. We have experimentally observed abundant spin-polarized edge states in the fractal lattice and demonstrated the robustness of topological edge states against defects. Although momentum space is ill defined, the propagating direction of edge states is still locked with the spin. Intriguingly, the lack of bulk sites not only does not hinder the existence of topological edge states but also increases the velocity of the sound transport in the fractal lattice.

Beyond the Sierpinski carpet, the spin Chern topological phase may also be observed in other fractal geometries,

e.g., Sierpinski gasket. In phononics, based on a spin Chern topological phase achieved in the kagome lattice [35], it is a feasible scheme to construct a nontrivial spin Chern topological phase in Sierpinski gasket. Recently, the Lieb lattice [43] and the Sierpinski gasket [44] have been experimentally fabricated in the electronic system by positioning carbon monoxide molecules on a Cu (111) surface. We predict that our design may also be experimentally verified in an electronic system. In photonic systems, the experimental observation of spin Chern insulator in the fractal lattice may also be possible in an array of coupled resonator optical waveguides [45]. Beyond the phononic systems, our study of the wave dynamics of the spin-polarized edge states in the fractal lattice may pave the way for designing multichannel on-chip communication devices [46,47].

Acknowledgments. This work was supported by the National Key Research and Development Program of China (Grants No. 2022YFA1404501 and No. 2021YFA1400601), the National Natural Science Fund for Distinguished Young Scholars (Grant No. 11925403), and the National Natural Science Foundation of China (Grants No. 12122406, No. 12192253, and No. 12304486).

- [1] B. Mandelbrot, How long is the coast of Britain? Statistical self-similarity and fractional dimension, *Science* **156**, 636 (1967).
- [2] A. N. D. Posadas, R. Quiroz, P. E. Zorogastúa, and C. León-Velarde, Multifractal characterization of the spatial distribution of ulexite in a Bolivian salt flat, *Int. J. Remote Sens.* **26**, 615 (2005).
- [3] E. Azpeitia, G. Tichtinsky, M. L. Masson, A. Serrano-Mislata, J. Lucas, V. Gregis, C. Gimenez, N. Prunet, E. Farcot, M. M. Kater *et al.*, Cauliflower fractal forms arise from perturbations of floral gene networks, *Science* **373**, 192 (2021).
- [4] R. M. Brady and R. C. Ball, Fractal growth of copper electrodeposits, *Nature (London)* **309**, 225 (1984).
- [5] D. H. Werner and S. Ganguly, An overview of fractal antenna engineering research, *IEEE Antennas Propag. Mag.* **45**, 38 (2003).
- [6] D. H. Werner, R. L. Haupt, and P. L. Werner, Fractal antenna engineering: The theory and design of fractal antenna arrays, *IEEE Antennas Propag. Mag.* **41**, 37 (1999).
- [7] H. Samavati, A. Hajimiri, A. R. Shahani, G. N. Nasserbakht, and T. H. Lee, Fractal capacitors, *IEEE J. Solid-State Circuits* **33**, 2035 (1998).
- [8] S. Alexander and R. Orbach, Density of states on fractals: \ll fractons \gg , *J. Phys. Lett.* **43**, 625 (1982).
- [9] R. Orbach, Dynamics of fractal networks, *Science* **231**, 814 (1986).
- [10] X. Y. Xu, X. W. Wang, D. Y. Chen, C. M. Smith, and X. M. Jin, Quantum transport in fractal networks, *Nat. Photonics* **15**, 703 (2021).
- [11] Z. Yang, E. Lustig, Y. Lumer, and M. Segev, Photonic Floquet topological insulators in a fractal lattice, *Light Sci. Appl.* **9**, 128 (2020).
- [12] T. Biesenthal, L. J. Maczewsky, Z. Yang, M. Kremer, M. Segev, A. Szameit, and M. Heinrich, Fractal photonic topological insulators, *Science* **376**, 1114 (2022).
- [13] M. Fremling, M. Van Hooff, C. M. Smith, and L. Fritz, Existence of robust edge currents in Sierpiński fractals, *Phys. Rev. Res.* **2**, 013044 (2020).
- [14] A. A. Iliasov, M. I. Katsnelson, and S. Yuan, Hall conductivity of a Sierpiński carpet, *Phys. Rev. B* **101**, 045413 (2020).
- [15] S. Fischer, M. van Hooff, T. van der Meijden, C. M. Smith, L. Fritz, and M. Fremling, Robustness of chiral edge modes in fractal-like lattices below two dimensions: A case study, *Phys. Rev. Res.* **3**, 043103 (2021).
- [16] J. Li, Y. Sun, Q. Mo, Z. Ruan, and Z. Yang, Fractality-induced topological phase squeezing and Devil's staircase, *Phys. Rev. Res.* **5**, 023189 (2023).
- [17] C. Liu, Y. Zhou, G. Wang, Y. Yin, C. Li, H. Huang, D. Guan, Y. Li, S. Wang, H. Zheng *et al.*, Sierpiński structure and electronic topology in Bi thin films on InSb(111)B surfaces, *Phys. Rev. Lett.* **126**, 176102 (2021).
- [18] S. Pai and A. Prem, Topological states on fractal lattices, *Phys. Rev. B* **100**, 155135 (2019).
- [19] S. Manna, S. Nandy, and B. Roy, Higher-order topological phases on fractal lattices, *Phys. Rev. B* **105**, L201301 (2022).
- [20] S. Zheng, X. Man, Z.-L. Kong, Z.-K. Lin, G. Duan, N. Chen, D. Yu, J.-H. Jiang, and B. Xia, Observation of fractal higher-order topological states in acoustic metamaterials, *Sci. Bull.* **67**, 2069 (2022).
- [21] J. Li, Q. Mo, J.-H. Jiang, and Z. Yang, Higher-order topological phase in an acoustic fractal lattice, *Sci. Bull.* **67**, 2040 (2022).
- [22] M. Li, C. Li, L. Yan, Q. Li, Q. Gong, and Y. Li, Fractal photonic anomalous Floquet topological insulators to generate multiple quantum chiral edge states, *Light Sci. Appl.* **12**, 262 (2023).
- [23] L. Fu and C. L. Kane, Time reversal polarization and a Z_2 adiabatic spin pump, *Phys. Rev. B* **74**, 195312 (2006).
- [24] R. Yu, X. L. Qi, A. Bernevig, Z. Fang, and X. Dai, Equivalent expression of Z_2 topological invariant for band insulators using the non-Abelian Berry connection, *Phys. Rev. B* **84**, 075119 (2011).
- [25] D. N. Sheng, Z. Y. Weng, L. Sheng, and F. D. M. Haldane, Quantum spin-Hall effect and topologically invariant Chern numbers, *Phys. Rev. Lett.* **97**, 036808 (2006).
- [26] C. L. Kane and E. J. Mele, Quantum spin Hall effect in graphene, *Phys. Rev. Lett.* **95**, 226801 (2005).
- [27] B. A. Bernevig, T. L. Hughes, and S.-C. Zhang, Quantum spin Hall effect and topological phase transition in HgTe quantum wells, *Science* **314**, 1757 (2006).
- [28] H. Li, L. Sheng, and D. Y. Xing, Connection of edge states to bulk topological invariance in a quantum spin Hall state, *Phys. Rev. Lett.* **108**, 196806 (2012).
- [29] B. Zhou, H.-Z. Lu, R.-L. Chu, S.-Q. Shen, and Q. Niu, Finite size effects on helical edge states in a quantum spin-Hall system, *Phys. Rev. Lett.* **101**, 246807 (2008).
- [30] H. Li, L. Sheng, D. N. Sheng, and D. Y. Xing, Chern number of thin films of the topological insulator Bi_2Se_3 , *Phys. Rev. B* **82**, 165104 (2010).
- [31] Y. Yang, Z. Xu, L. Sheng, B. Wang, D. Y. Xing, and D. N. Sheng, Time-reversal-symmetry-broken quantum spin Hall effect, *Phys. Rev. Lett.* **107**, 066602 (2011).
- [32] E. Prodan, Robustness of the spin-Chern number, *Phys. Rev. B* **80**, 125327 (2009).
- [33] E. Prodan, Non-commutative tools for topological insulators, *New J. Phys.* **12**, 065003 (2010).
- [34] W. Deng, X. Huang, J. Lu, V. Peri, F. Li, S. D. Huber, and Z. Liu, Acoustic spin-Chern insulator induced by synthetic spin-orbit coupling with spin conservation breaking, *Nat. Commun.* **11**, 3227 (2020).
- [35] Y. Yang, J. Lu, M. Yan, X. Huang, W. Deng, and Z. Liu, Hybrid-order topological insulators in a phononic crystal, *Phys. Rev. Lett.* **126**, 156801 (2021).
- [36] H. Liu, B. Xie, H. Wang, W. Liu, Z. Li, H. Cheng, J. Tian, Z. Liu, and S. Chen, Acoustic spin-Chern topological Anderson insulators, *Phys. Rev. B* **108**, L161410 (2023).
- [37] H. Huang and F. Liu, Quantum spin Hall effect and spin Bott index in a quasicrystal lattice, *Phys. Rev. Lett.* **121**, 126401 (2018).
- [38] H. Huang and F. Liu, Theory of spin Bott index for quantum spin Hall states in nonperiodic systems, *Phys. Rev. B* **98**, 125130 (2018).
- [39] D. Toniolo, On the Bott index of unitary matrices on a finite torus, *Lett. Math. Phys.* **112**, 126 (2022).
- [40] See Supplemental Material at <http://link.aps.org/supplemental/10.1103/PhysRevB.109.L140104> for (I) Calculation of the spin Bott index, (II) topological phase of Lieb lattice phononic crystal, (III) spectrum of $G(2)$ and $G(3)$ Sierpinski carpet, (IV) velocity measurement in the Lieb lattice, (V)

- propagation direction of edge state in Sierpinski carpet, (VI) the increasing velocity of the edge state, and (VII) details for experiments, which includes Refs. [41,42].
- [41] M. B. Hastings and T. A. Loring, Almost commuting matrices, localized Wannier functions, and the quantum Hall effect, *J. Math. Phys.* **51**, 015214 (2010).
- [42] B. I. Halperin, Quantized Hall conductance, current-carrying edge states, and the existence of extended states in a two-dimensional disordered potential, *Phys. Rev. B* **25**, 2185 (1982).
- [43] M. R. Slot, T. S. Gardenier, P. H. Jacobse, G. C. P. Van Miert, S. N. Kempkes, S. J. M. Zevenhuizen, C. M. Smith, D. Vanmaekelbergh, and I. Swart, Experimental realization and characterization of an electronic Lieb lattice, *Nat. Phys.* **13**, 672 (2017).
- [44] S. N. Kempkes, M. R. Slot, S. E. Freeney, S. J. M. Zevenhuizen, D. Vanmaekelbergh, I. Swart, and C. M. Smith, Design and characterization of electrons in a fractal geometry, *Nat. Phys.* **15**, 127 (2019).
- [45] M. Hafezi, E. A. Demler, M. D. Lukin, and J. M. Taylor, Robust optical delay lines with topological protection, *Nat. Phys.* **7**, 907 (2011).
- [46] J. Cha, K. W. Kim, and C. Daraio, Experimental realization of on-chip topological nanoelectromechanical metamaterials, *Nature (London)* **564**, 229 (2018).
- [47] Y. Yang, Y. Yamagami, X. Yu, P. Pitchappa, J. Webber, B. Zhang, M. Fujita, T. Nagatsuma, and R. Singh, Terahertz topological photonics for on-chip communication, *Nat. Photonics* **14**, 446 (2020).